A Novel Miniaturized Multiband Strong Coupled-FSS Structure Insensitive to Almost All Angles and All Polarizations

Tian-Wu Li, Yu-Di Fan, Yi-Jie Gu, Shi-Yun Zhou, Peng-Fei Qin, Da Li, Wei E. I. Sha, *Senior Member, IEEE*, and Er-Ping Li, *Fellow, IEEE*

***Abstract*— This article presents a novel miniaturized almost all-angle-insensitive strong coupled frequency-selective surface (SC-FSS) with all-polarization-insensitive multiband by introducing the different interlayer coupling patches. Two templates of a single passband and a dual passband with unit cell less than 0.03λ are adopted to bring in two stopbands on both ends of each passband. Furthermore, the corresponding equivalent circuit models are developed to explain the physical mechanism and formulate relevant design equations. Finally, a prototype of the proposed dual-passband structure is fabricated and measured to verify the results of full-wave simulation and theoretical analysis. The experiment results show that there are a lower passband working at 2 GHz and a higher passband at 5.8 GHz with a lower stopband at 4 GHz and a higher at 7.5 GHz at the ends of above passbands, respectively, which exhibits the stable performance against the variation of the incident angles (from 0° to 86°) for both TE and TM polarizations. The measurement results demonstrate that the proposed multiband SC-FSS is a good candidate for designing a high-performance antenna radome for solving electromagnetic interference (EMI) problems.**

***Index Terms*— All-angle-insensitive, all-polarization-insensitive, equivalent circuit model (ECM), multiband, strong coupled frequency-selective surface (SC-FSS).**

I. Introduction

FREQUENCY-SELECTIVE surface (FSS) is an artificial periodic structure [1], [2], which has been extensively utilized in a wide range of applications, such as electromagnetic interference (EMI) shielding, absorbers, antenna reflectors, and hybrid high-performance radomes [3]–[11]. In the modern complex wireless communication systems, the increasing demands for multitude of emerging communication systems require that the multifunctional antennas work well in multiple frequency bands. Thus, the research of high-selective multiband FSS attracts more attention.

In previous studies, FSS structures with multiple independent passbands or stopbands have been realized in different approaches. By cascading a 2-D periodic array of double square loops and an array of gridded square loops based on microwave filter theory, Li and Shen [12] designed a quasi-elliptic passband FSS, and Yan *et al.* [13]–[15] have realized highly selective dual-band, triband, and quad-band FSS structures. Payne *et al.* [16] proposed a semianalytic technique for synthesizing thin dual-passband FSS derived from a classical filter theory. In addition, fractal structures are also utilized in the design of high-order or multiband FSS [17], [18]. However, the resonant mechanism of these structures is based on the half-wavelength resonance of wave physics, which limits structure miniaturization. Also, as we all know, the responses of FSS are not only a function of frequency but also a function of the incident angle and polarization. At oblique incidence, the problem of grating lobe and frequency offset may occur in the above structures, which can work well only under the incident angle range less than 60° even than 45°. Although several works have achieved good angle stability, they exhibit only single-band structures [19], [20]. Li *et al.* [21] designed the dual passband with large band ratios by using 3-D FSS. While it can work well only in single polarization, there is a serious frequency offset in higher passband. Therefore, an ultraminiaturized, all-angle and polarization-insensitive multiband FSS structure is highly desirable.

This article presents a new kind of miniaturized multiband FSS insensitive to all incident angles and polarizations based on strong coupled frequency-selective surface (SC-FSS). Inspired by the design of 2.5-D and 3-D FSS which can enhance the effective inductance using the vertical space [22]–[24], SC-FSS is developed with strong coupled capacitances in the *z*-direction. First, a single passband working at 3.7 GHz with two stopbands at 2 and 5 GHz at both ends of passband is designed by introducing two different interlayer coupling patches. Even when the incident angle varieties in

Manuscript received March 8, 2020; revised November 21, 2020; accepted December 5, 2020. Date of publication October 8, 2021; date of current version December 16, 2021. This work was supported in part by the National Natural Science Foundation of China under Grant 62071424 and Grant 62027805, in part by the Zhejiang Laboratory Foundation of China under Grant 2020KCDAB01, and in part by the Zhejiang Provincial Natural Science Foundation of China under Grant LD21F010002. *(Corresponding author: Er-Ping Li.)*

Tian-Wu Li, Yi-Jie Gu, Shi-Yun Zhou, Peng-Fei Qin, Da Li, and Wei E. I. Sha are with the Key Laboratory of Advanced Micro-Nano Electronic Devices and Smart Systems and Applications, College of Information Science and Electronic Engineering, Zhejiang University, Hangzhou 310027, China (e-mail: litianwu@zju.edu.cn).

Yu-Di Fan and Er-Ping Li are with the Key Laboratory of Advanced Micro-Nano Electronic Devices and Smart Systems and Applications, College of Information Science and Electronic Engineering, Zhejiang University, Hangzhou 310027, China, and also with the Zhejiang University–University of Illinois at Urbana–Champaign Institute, Zhejiang University, Haining 314400, China (e-mail: liep@zju.edu.cn).

Color versions of one or more figures in this article are available at https://doi.org/10.1109/TAP.2021.3063351.

Digital Object Identifier 10.1109/TAP.2021.3063351

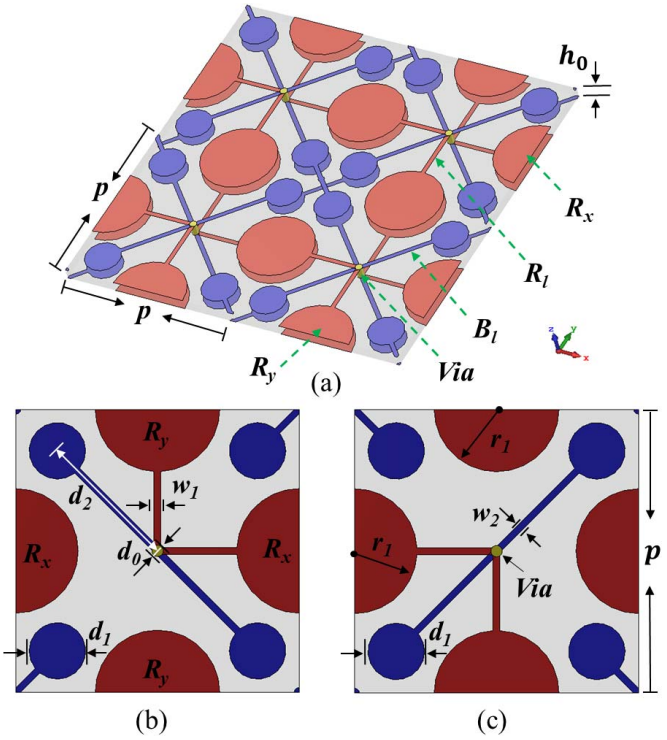

Fig. 1. Schematic of the proposed all-angle and polarization-insensitive SC-FSS structure with dual stopband and its unit cell. (a) 3-D view. (b) Bottom layer. (c) Top layer. Optimized geometric parameters are: $p = 4.5$ mm, $h_0 = 0.1$ mm, $\varepsilon_r = 10.2$, $d_0 = 0.1$ mm, $r_1 = 1.08$ mm, $w_1 = 0.1$ mm, $w_2 = 0.1$ mm, $d_1 = 0.92$ mm, and $d_2 = p/2$.

the range of nearly 90°, the resonant frequencies remain constant for both TE and TM modes. In addition, an almost all-angle and polarization-insensitive dual-passband SC-FSS is developed from the single-passband structure by introducing a meandered strip metal structure in the bottom layer, which can be regarded as a parallel inductance. Furthermore, the field and surface current distribution patterns of the proposed structures are investigated and the corresponding equivalent circuit model (ECM) is also developed to analyze the physical mechanism and formulate relevant design equations. Finally, to verify the proposed method, a prototype of the proposed dual-passband structure is measured where the measurement results are consistent with the simulated ones by CST and ECM.

II. Highly Selective Single-Passband SC-FSS

A. Structure Description

The proposed SC-FSS structure consists of two metal layers attached on both sides of a very thin dielectric layer, as shown in Fig. 1(a). There are only four unit cells presented as a conceptual model for the sake of simplicity. Fig. 1(b) and (c) shows the bottom and top layers of the unit cell, respectively. The bottom layer is divided into red and blue areas, in which the red area contains four semicircles ($\boldsymbol{R_x}$, $\boldsymbol{R_y}$) and two rectangular patches ($\boldsymbol{R_l}$) and the blue area is composed of four circles and rectangular patches ($\boldsymbol{B_l}$) connected with circles. The top layer is the corresponding but rotationally symmetric geometry of the bottom one. Furthermore, it is essential for angular stability that the metal via ($\boldsymbol{V_{ia}}$) is designed to connect the structures of top and bottom layers at the center of the unit cell. Taconic RF-10 with a permittivity $\boldsymbol{\varepsilon_r}$ of 10.2 and a tangent loss tan δ of 0.0025 is used as the dielectric layer.

B. Operation Principle

In order to make the proposed FSS structure insensitive to the incident angles, the strong coupling between the top and bottom layers is introduced by designing the specific position relations of structures. Besides, with the influence of the middle dielectric layer, when the incident electromagnetic waves reach the surface of the structure, it can be regarded as the parallel-plate capacitance at a specific frequency, which is much larger than the equivalent capacitance generated by the structure coupling in the same layer. In addition, even if the incident angle changes, the structure still maintains a stable mode at the resonant frequency, which makes it insensitive to the incident angle.

To obtain a higher selectivity, it is expected to design a passband FSS structure with the stopbands at both ends of the passband. As shown in Fig. 1, there are two sizes of metal circular patches, which can form two stopbands before and after the passband. Also, they work together to control the central passband, which ensures excellent structural selectivity. To further understand and analyze the physical mechanism, the distributions of electric field in the middle of dielectric layer and surface current on each metal layer at their respective resonance frequencies are shown in Fig. 2.

The electric field distributions at lower stopband for TE mode are presented in Fig. 2(a_1) and (b_1), where the electric field is completely bound between two red circular patches $\boldsymbol{R_y}$, forming a strong coupling in the z-direction. At the circuit level, this strong coupling can be equivalent to a large capacitance $\boldsymbol{C_{s1}}$. At the same time, the current is mainly distributed on red rectangular patches $\boldsymbol{R_l}$, which introduces an inductance $\boldsymbol{L_1}$. Also, the vias connecting the top and bottom layers can be regarded as another inductance $\boldsymbol{L_v}$. Those vias are very important for the angular stability because they change the resonant mechanism from the wave physics to circuit physics. Correspondingly, when the structure is excited by x-polarization waves, the electric fields and currents are mainly distributed in red circular patches $\boldsymbol{R_x}$ and red rectangular patches in the x-direction. The equivalent capacitance $\boldsymbol{C_{s1}}$ and inductance $\boldsymbol{L_{s1}}$ ($\boldsymbol{L_{s1} = L_1 + L_v}$) form an $\boldsymbol{LC}$ series resonance at the resonant frequency $\boldsymbol{f_{s1}}$ working as lower stopband. It is demonstrated that the lower stopband is determined by the red part of the structure in Fig. 1, and we can adjust the parameters of the red part to optimize the desired lower stopband.

The working mechanism of the higher stopband is consistent with that of the lower stopband. The electric field distributions of higher stopband (at the middle of dielectric layer) and surface current (on all layers) at 5 GHz are shown in Fig. 2(a_2) and (b_2), respectively. In this case, the electric field is concentrated on smaller blue circular patches and the current mainly flows on the blue rectangular patches ($\boldsymbol{B_l}$) connected with smaller blue circular patches, which can be equivalent to a capacitance $\boldsymbol{C_{s2}}$ and an inductance $\boldsymbol{L_2}$,

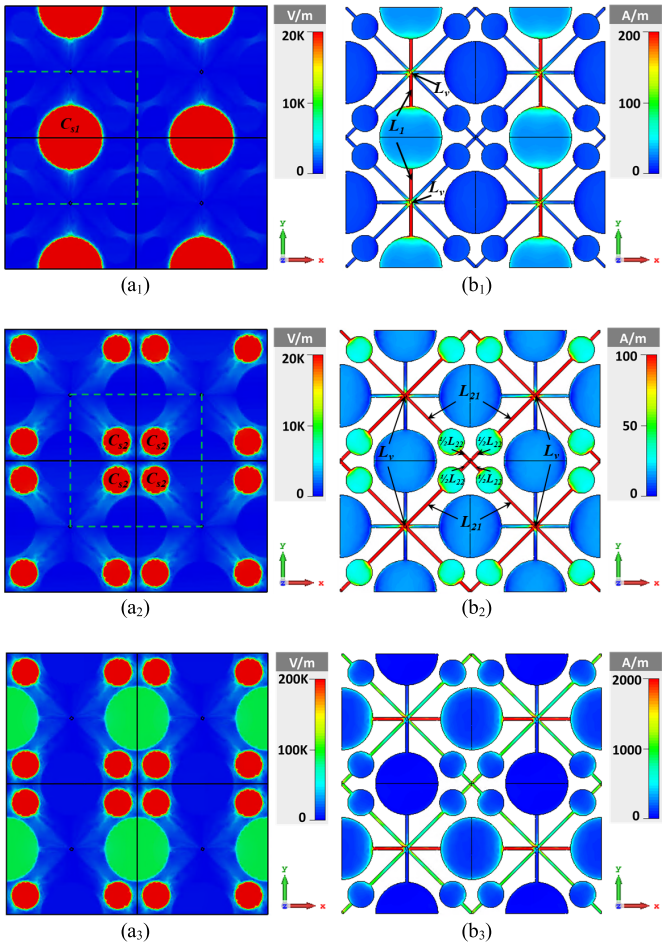

Fig. 2. Distributions of electric field (at the middle of dielectric layer) and surface current (on all metal layers). The first column shows electric field distributions and the second column displays surface current distributions. (a_1) and (b_1) Working as lower stopband at 2 GHz for TE mode. (a_2) and (b_2) Working as higher stopband at 5 GHz for TE mode. (a_3) and (b_3) Working as the passband at 3.7 GHz for TM mode.

respectively. The capacitance C_{s2} and the inductance L_{s2} ($L_{s2} = L_2 + L_v$) form another LC series resonance at resonant frequency f_{s2} working as higher stopband. As a result, higher stopband is dependent on the blue parts of structure in Fig. 1.

From Fig. 2(a_3) and (b_3), it is observed that the electric field distributions and surface currents for TM mode at 3.7 GHz working as the central passband are distributed on both full smaller blue circular patches and larger red ones (R_x), which introduces two capacitances C_{s2} and C_{s1}. Meanwhile, the surface currents are concentrated on all blue rectangular patches (B_l) and red ones (R_l) in the x-direction, which can be considered as the inductances L_2 and L_1. Two LC series resonant circuits mentioned above form a new LC parallel circuit to realize the central passband. Therefore, the whole structure controls the passband of the proposed FSS.

According to the analysis above, an ECM is proposed as shown in Fig. 3(a), where the parameters are calculated by empirical formulas (1)–(9) based on the research in [23] and [29]. In particular, considering the influence of the fringing electric field, a correction factor R_e given in [25] is improved

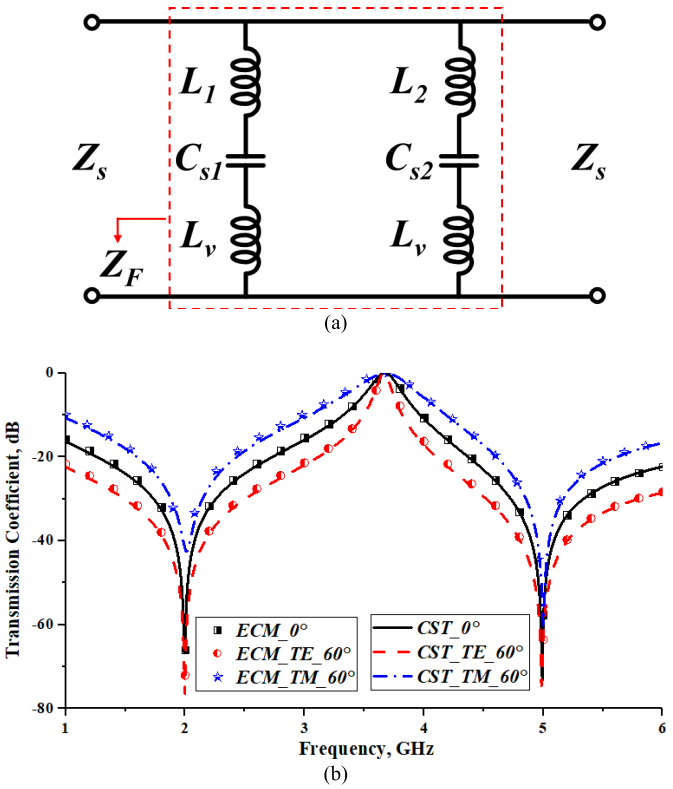

Fig. 3. (a) Proposed ECM. (b) Simulation results of ECM in comparison with those by CST. The difference between the calculated values of the circuital parameters (1)–(9) and optimized ones by fitting in ADS is shown in Table I.

TABLE I

COMPARISON OF NUMERICAL CALCULATION RESULTS WITH THE FITTING AND OPTIMIZED ONES BY ADS

	L_1 (nH)	L_v (nH)	L_{s1} (nH)	L_{21} (nH)	½ L_{22} (nH)	L_{s2} (nH)
Fitting by ADS	\	\	1.908	\	\	1.598
Numerical calculation	1.80	0.048	1.848	1.281	0.277	1.606
Error coefficient	\	\	-3.1%	\	\	0.5%

	C_{s1} (pf)	C_{s2} (pf)	f_{s1} (GHz)	f_{s2} (GHz)	f_p (GHz)
Fitting by ADS	3.33	0.64	1.997	4.977	3.669
Simulation by CST	\	\	2.00	4.990	3.67
Numerical calculation	3.396	0.631	2.009	5.001	3.713
Error coefficient	2.0%	-1.4%	0.5%	0.2%	1.1%

to calculate a more accurate capacitance value

$$C_{s1} = \frac{\varepsilon_0 \varepsilon_r \pi R_{e1}^2}{h_0} \tag{1}$$

$$R_{e1} = r_1\left(1 + \frac{2h_0}{\pi r_1 \varepsilon_r}\left(ln\left(\frac{\pi r_1}{2h_0}\right) + 1.7726\right)\right)^{1/2} \tag{2}$$

$$L_1 = \mu_0 \frac{p - 2r_1}{2\pi} ln\left(\frac{2(p - 2r_1)}{w_1}\right) \tag{3}$$

$$L_v = 200h_0\left(1 + ln\left(\frac{4h_0}{d_0}\right)\right) \cdot 10^{-9} \tag{4}$$

$$C_{s2} = \frac{\varepsilon_0 \varepsilon_r \pi R_{e2}^2}{h_0} \tag{5}$$

$$R_{e2} = \frac{d_1}{2}\left(1 + \frac{4h_0}{\pi d_0 \varepsilon_r}\left(ln\left(\frac{\pi d_1}{4h_0}\right) + 1.7726\right)\right)^{1/2} \tag{6}$$

$$L_{21} = \mu_0 \frac{0.5p - 0.5d_1}{2\pi} ln\left(\frac{2(0.5p - 0.5d_1)}{w_2}\right) \tag{7}$$

$$L_{22} = \mu_0 \frac{\sqrt{2}p - 2d_2 - d_1}{2\pi} ln\left(\frac{2\left(\sqrt{2}p - 2d_2 - d_1\right)}{w_2}\right) \tag{8}$$

$$L_2 = L_{21} + 0.5L_{22}. \tag{9}$$

The equivalent impedance Z_F of the proposed FSS structure is given as follows:

$$Z_F = \frac{\left(1 - \omega^2 C_{s1} L_{s1}\right)\left(1 - \omega^2 C_{s2} L_{s2}\right)}{j\omega\left(C_{s1} + C_{s2} - \omega^2 C_{s1} C_{s2} L_{s1} - \omega^2 C_{s1} C_{s2} L_{s2}\right)} \tag{10}$$

$$L_{s1} = L_1 + L_v \tag{11}$$

$$L_{s2} = L_2 + L_v. \tag{12}$$

Based on the transmission line theory, when $\boldsymbol{Z_F}$ tends to zero, the electromagnetic waves are fully reflected and the transmission zeros $\boldsymbol{f_{s1}}$ and $\boldsymbol{f_{s2}}$ can be obtained as expressed in formulas (13) and (14). Analogously, as $\boldsymbol{Z_F}$ goes to infinity, we can calculate the transmission pole $\boldsymbol{f_p}$ as presented formulas (15), which signifies that the EM waves can pass through the structure.

$$f_{s1} = \frac{1}{2\pi} \cdot \sqrt{\frac{1}{L_{s1} C_{s1}}} \tag{13}$$

$$f_{s2} = \frac{1}{2\pi} \cdot \sqrt{\frac{1}{L_{s2} C_{s2}}} \tag{14}$$

$$f_p = \frac{1}{2\pi} \cdot \sqrt{\frac{C_{s1} + C_{s2}}{(L_{s1} + L_{s2}) C_{s1} C_{s2}}}. \tag{15}$$

C. Simulation Results

Based on the work described above, a large number of data fitting operations are carried out, and the optimized ECM as shown in Fig. 3(a) is simulated by the circuit simulation software ADS. Fig. 3(b) shows the comparison results obtained by ECM and using the EM simulation software CST Microwave Studio. It is observed from the figure that the ECM results are consistent with full-wave simulation ones, which confirms that the above analysis is practicable. In addition, we obtain the angular response of the ECM for different polarizations and angles by changing the free-space impedance of incident waves Z_s (Z_s changes with $Z_0/cos(\theta)$ for TE mode, while it varies to $Z_0^* cos(\theta)$ for TM mode, where $Z_0 = 377\ \Omega$). Since the designed FSS structure is insensitive to the incident angles and polarizations, the proposed ECM can completely characterize the angular response of the proposed structure, which guides us to further understand the working mechanism and optimize the design of the subsequent structure.

Furthermore, the transmission spectra of the proposed FSS structure under different polarizations and incident angles are shown in Fig. 4. There is a highly selective passband working at 3.7 GHz with a lower stopband working at 2 GHz and a higher stopband at 5GHz at both ends of passband. It is worth mentioning that the transmission poles $\boldsymbol{f_p}$ are always stable at 3.7 GHz, and the two transmission zeros $\boldsymbol{f_{s1}}$ and $\boldsymbol{f_{s2}}$ are also kept at 2 and 5 GHz, respectively, even when the incident angle changes to nearly 90° for both TE and TM modes. Therefore, these results demonstrate that the proposed structure has excellent selectivity and is completely insensitive to all angles and all polarizations, which can be applied to the design of high-performance radome or antenna reflector in the communication system.

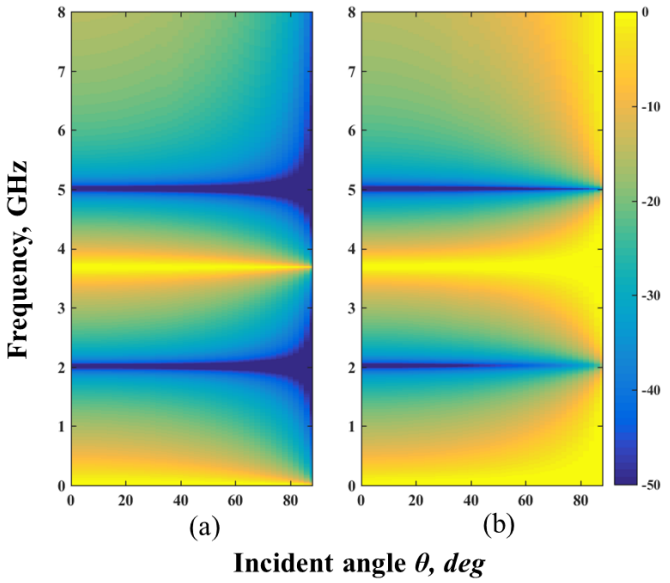

Fig. 4. Transmission spectra of the proposed dual-stopband SC-FSS structure. (a) TE mode. (b) TM mode.

III. All-Angle and Polarization-Insensitive Dual-Passband SC-FSS

A. Structure Description

Fig. 5 shows the schematic of the proposed almost all-angle and polarization-insensitive SC-FSS structure with dual passband, which is developed from the highly selective single-passband SC-FSS described in Section II. In addition to the excellent angle and polarization stability and high selectivity, it is noted that this structure can function well with dual passband at sub-6 GHz. In this design, each unit cell consists of three metal layers that are separated by a thinner dielectric $\boldsymbol{D_1}$ and a thicker one $\boldsymbol{D_2}$. The first two metal layers of this structure are similar to those of the previous single-passband structure, which also consists of two kinds of coupling metal patches and the rectangular patches connected with them. What difference is that the analogous capsule metal patches are designed to replace the original smaller circular ones to further enhance the interlayer coupling. In order to obtain the dual passband at sub-6 GHz, we cascade a meandered strip metal structure at the bottom layer, as shown in Fig. 5(d). Similarly, the metal vias ($\boldsymbol{V_{ia}}$) are loaded in the center of unit cell to connect the three metal layers together. The details and optimized geometric parameters are shown in Fig. 5(b)–(d).

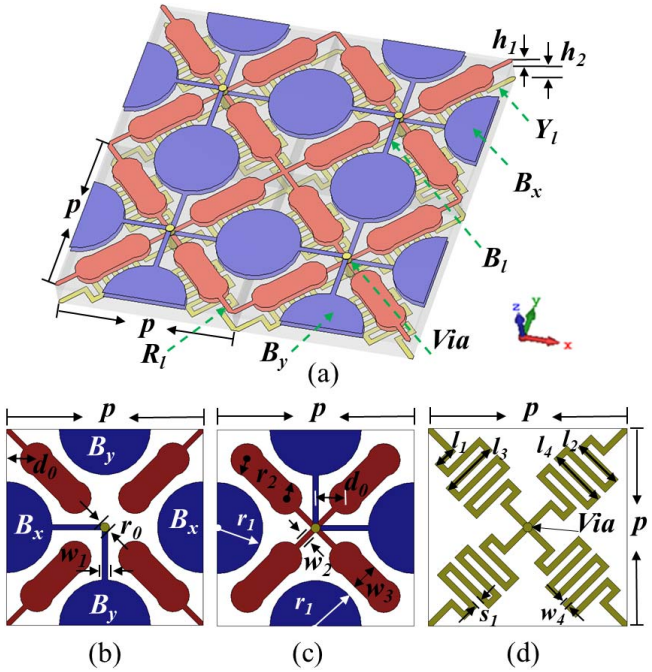

Fig. 5. Schematic of the proposed all-angle and polarization-insensitive SC-FSS structure with dual passband and its unit cell. (a) 3-D view. (b) Top layer. (c) Second layer. (d) Bottom layer. Optimized geometric parameters are: $p = 4.3$ mm, $h_1 = 0.101$ mm, $h_2 = 0.355$ mm, $r_0 = 0.2$ mm, $r_1 = 0.98$ mm, $w_1 = 0.12$ mm, $r_2 = 0.33$ mm, $w_2 = 0.12$ mm, $w_3 = 0.66$ mm, $w_4 = 0.13$ mm, $l_1 = 0.52$ mm, $l_2 = 1.1$ mm, $l_3 = 1.3$ mm, $l_4 = 1.3$ mm. $s_1 = 0.14$ mm, and $d_0 = 0.355$ mm.

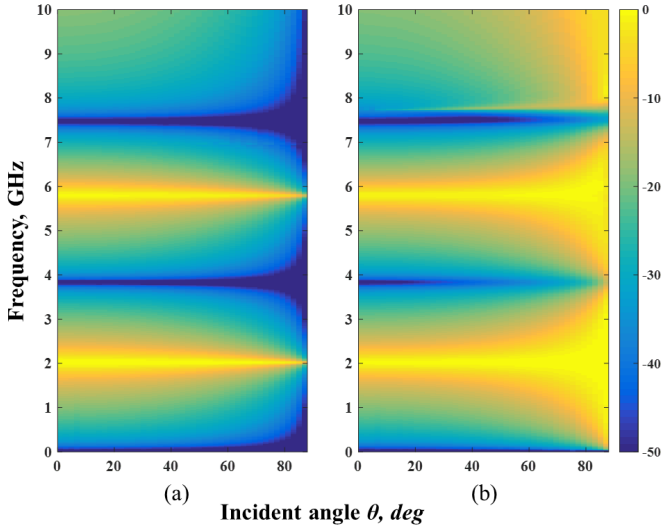

Fig. 6. Transmission spectra of the proposed dual-passband SC-FSS structure. (a) TE mode. (b) TM mode.

B. Operation Principle and Simulation

The transmission spectrum of the proposed almost all-angle and polarization-insensitive dual-passband SC-FSS structure under different incident angles (0°–88°, step = 2°) for both TE and TM modes is extracted, as shown in Fig. 6. It is obvious that there is a highly selective lower passband at 2 GHz and a higher one at 5.8 GHz with a lower stopband at 3.8 GHz and a higher one at 7.4 GHz at the ends of both lower and higher passbands. Regardless of any passband or stopband, all resonant frequencies remain constant for both TE and TM modes, even if the incident angle increases to 88°.

In order to further understand the operation principle of this structure, we investigate the field and surface current distribution patterns of this structure (see Fig. 7), in which the field modes and current distributions at the three resonant frequencies are consistent with those of the single-passband FSS structure presented in Section II. Correspondingly, the lower stopband working at 3.8 GHz is controlled by the blue parts of the structure shown in Fig. 5, while the higher stopband working at 7.4 GHz depends on the red parts. Also, the red and blue parts together mainly determine the performance of higher passband working at 5.8 GHz. It is clearly observed from Fig. 7(a_1) that the electric fields are mainly concentrated on the larger blue circular patches, while the distribution on the red analogous capsule patches is relatively weak. Simultaneously, the surface currents mainly flow on the rectangular patches ($\boldsymbol{B_l}$) connected with larger blue circular patches and the whole bottom yellow metal structure. As a result, the lower passband is mainly determined by the blue and yellow parts of the structure, while the influence of red part is limited. In circuit level, the equivalent $\boldsymbol{LC}$ series circuit of the blue part and the inductance $\boldsymbol{L_p}$ introduced by the bottom yellow part form a new $\boldsymbol{LC}$ parallel circuit, which characterizes the performance of lower passband. Also, the complete ECM of this structure is proposed, as shown in Fig. 8(a). The equivalent impedance $\boldsymbol{Z_F}$ of the proposed FSS structure is given in (16)–(18), as shown at the bottom of the next page.

Based on the transmission line theory mentioned in Section II, the transmission zeros $\boldsymbol{f_{s1}}$ and $\boldsymbol{f_{s2}}$ and the transmission poles $\boldsymbol{f_{p1}}$ and $\boldsymbol{f_{p2}}$ are calculated as follows:

$$f_{s1} = \frac{1}{2\pi} \cdot \sqrt{\frac{1}{(L_1 + L_v)C_{s1}}} \tag{19}$$

$$f_{s2} = \frac{1}{2\pi} \cdot \sqrt{\frac{1}{(L_2 + L_v)C_{s2}}} \tag{20}$$

$$f_{p1} = \frac{1}{2\pi} \cdot \sqrt{\frac{-B - \sqrt{B^2 - 4A}}{2A}} \tag{21}$$

$$f_{p2} = \frac{1}{2\pi} \cdot \sqrt{\frac{-B + \sqrt{B^2 - 4A}}{2A}} \tag{22}$$

where the variables $\boldsymbol{A}$ and $\boldsymbol{B}$ are expressed as

$$A = (C_{s1}C_{s2})\big(L_p(L_{s1} + L_{s2}) + L_{s1}L_{s2}\big) \tag{23}$$

$$B = -\big(L_p(C_{s1} + C_{s2}) + C_{s1}L_{s1} + C_{s2}L_{s2}\big). \tag{24}$$

Here, all inductances and capacitances are calculated by formulas (1)–(9) with the corresponding adjustment of internal structure parameters, and the optimal equivalent discrete parameters of the model are obtained as follows: $\boldsymbol{C_{s1}} = 1.28$ pF, $\boldsymbol{L_{s1}} = 1.34$ nH, $\boldsymbol{C_{s2}} = 0.49$ pF, $\boldsymbol{L_{s2}} = 0.94$ nH, and $\boldsymbol{L_p} = 2.78$ nH. It is obvious that all corresponding curves obtained by ECM and CST nearly overlap each other, which clearly demonstrates that the transmission performance

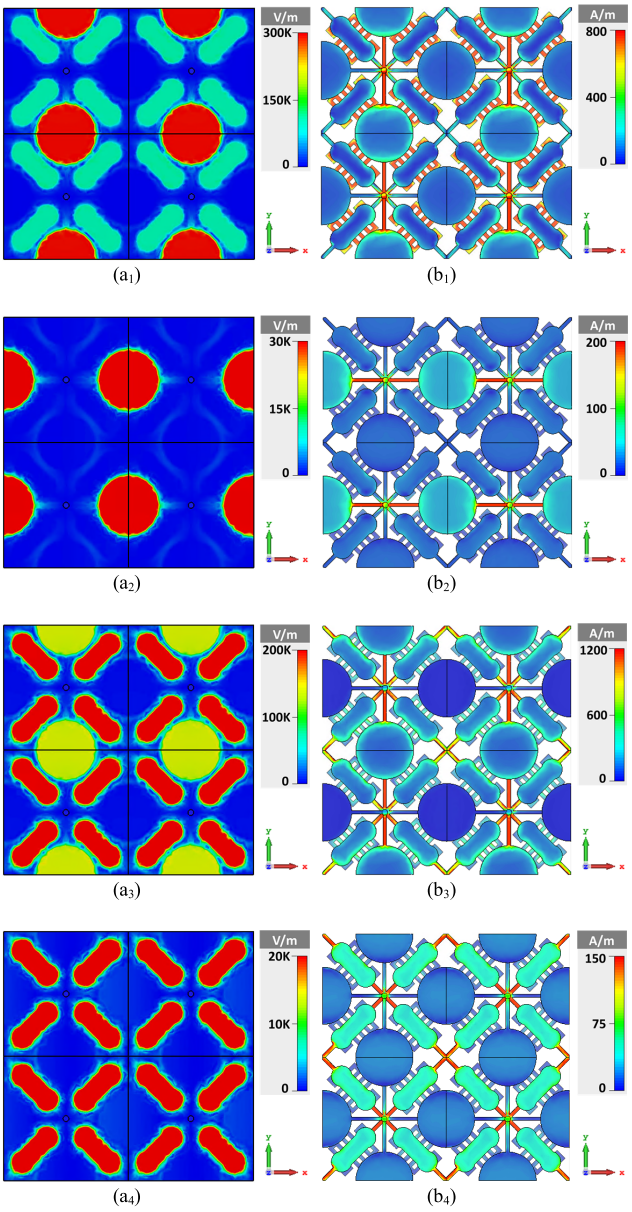

Fig. 7. Electric field distributions (at the middle of dielectric layer) and surface current (on all metal layers). The first column shows electric field distributions and the second column displays surface current distributions. (a_1) and (b_1) Lower passband at 2 GHz for TE mode. (a_2) and (b_2) Lower stopband at 3.8 GHz for TM mode. (a_3) and (b_3) Higher passband at 5.8 GHz for TE mode. (a_4) and (b_4) Higher stopband at 7.4 GHz for TM mode.

of the proposed structure under all incident angles and all polarizations can be fully equivalent by the extracted ECM.

C. Implementation and Experimental Verification

To experimentally validate the proposed methodology, a prototype structure and the measurement schematic are presented in Fig. 9. The prototype consists of three metallic layers etched on two sheets of dielectric substrate (Roger RT4350B with permittivity $\boldsymbol{\varepsilon}_r = 3.66$ and tangent loss $\boldsymbol{tan}\ \delta = 0.0037$) whose thicknesses are 0.101 and 0.254 mm,

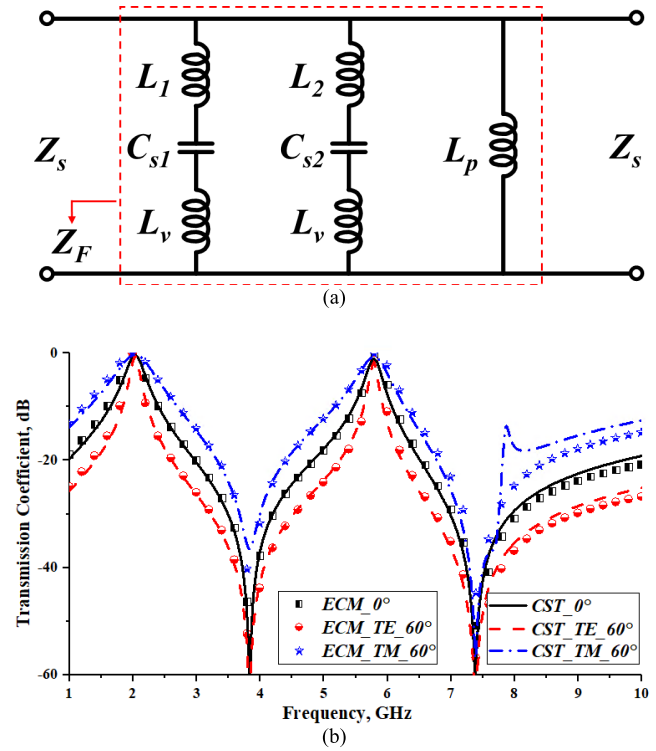

Fig. 8. (a) Proposed ECM. (b) Simulation results of ECM in comparison with those by CST.

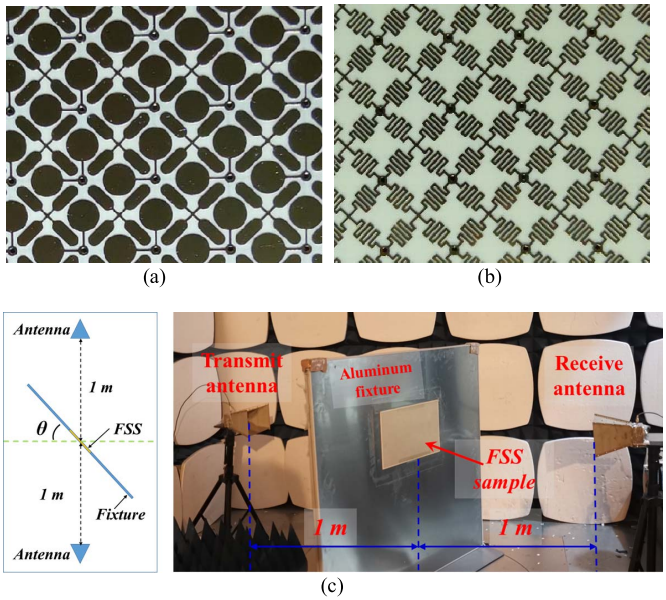

Fig. 9. Photograph of the fabricated FSS. (a) Top layer. (b) Bottom layer. (c) Schematic of measurement.

$$Z_F = \frac{j\omega L_p\left(1-\omega^2 C_{s1}L_{s1}\right)\left(1-\omega^2 C_{s2}L_{s2}\right)}{\left(1-\omega^2 C_{s1}L_{s1}\right)*\left(1-\omega^2 C_{s2}L_{s2}\right)-\omega^2 L_p C_{s1}\left(1-\omega^2 C_{s2}L_{s2}\right)-\omega^2 L_p C_{s2}\left(1-\omega^2 C_{s1}L_{s1}\right)} \tag{16}$$

$$L_{s1} = L_1 + L_v \tag{17}$$

$$L_{s2} = L_2 + L_v. \tag{18}$$

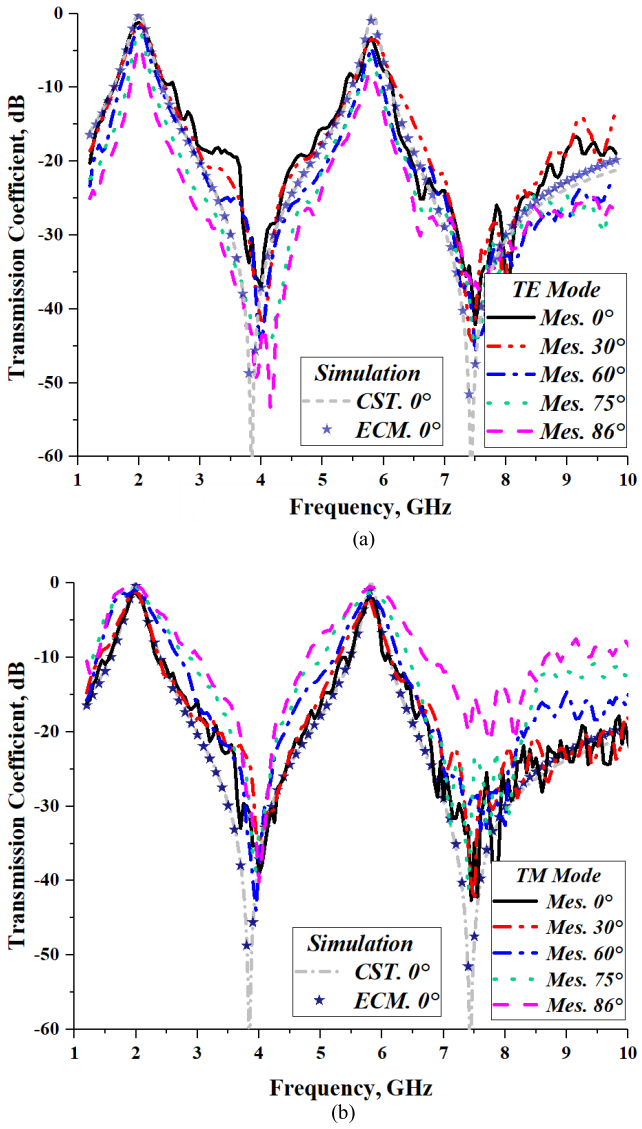

Fig. 10. Measurement results of the proposed dual-passband SC-FSS and the comparison with those by CST and ECM. (a) TE mode. (b) TM mode.

respectively. The dimension of the prototype is 280 mm × 430 mm containing 63 × 97 units, while the thickness of the metal layer is 35 μm. The unit cell is only 0.03λ, which is very beneficial for angular stability. Due to the actual processing limitations, we have no way to process a large enough FSS board. Considering that the board is not large enough, there would be an edge diffraction problem under oblique incidence, which affects the transmission performance of FSS. Thus, we designed a metal fixture as shown in Fig. 9(c) to prevent edge diffraction. The experimental setup is the same as that described in [26] where a pair of standard horn antennas HD-10180 connected to a vector network analyzer ZVA67 and the prototype is measured in the microwave anechoic chamber using the free-space transmission measurement method. Measurements with and without the FSS sample are implemented for the transmission coefficient calculation under each incident angle. Fig. 10(a) and (b) shows the transmission responses at different angles for TE and TM modes, respectively. It is observed that the measured results exhibit the predicted transmission poles of the dual-passband performance around 2 and 5.8 GHz, which agrees well with the simulated ones. Due to the fabrication errors and deviation of the dielectric properties, there is a slight shift of the transmission zeros compared to simulation. Furthermore, the transmission poles and zeros remind unchanged under different polarizations and the incident angles up to 86°. To further confirm the superiority of the proposed method, a performance comparison of previously multiband and miniaturized FSS designs with the proposed structure in this article is listed in Table II. It is concluded that no work in existing studies has realized the performance of dual-passband SC-FSS insensitive to quasi-all angles and all polarizations. In addition, the presented design also shows the advantages of ultraminiaturized unit cell size and ultrathin thickness in contrast with other similar works.

TABLE II
CHARACTERISTICS OF DIFFERENT FSS DESIGNS

FSS designs	Resonance frequency	Thickness	Unit cell	Angular stability	Angle response of resonance frequency
Structure in [15]	7.5, 12.5 & 19 GHz	2 mm	5 mm 0.125λ	60° for dual polarization	offset
Structure in [27]	4 & 7 GHz	3.15 mm	9.5 mm 0.08λ	45° for single polarization	Unchanged for TE mode
Structure in [21]	0.97 & 14.9 GHz	10.4 mm	9 mm 0.03λ	45° for single polarization	Higher passband offset
Structure in [28]	3.1 & 4.4 GHz	0.5 mm	6.25mm 0.065λ	60° for dual polarization	Unchanged for TE mode Changed for TM mode
Structure in [19]	Single band 2 GHz	0.26 mm	4.3 mm 0.029λ	84° for dual polarization	Unchanged
Proposed structure	**2, 3.8, 5.8 & 7.4 GHz**	**0.46 mm**	**4.3 mm 0.029λ**	**86° for dual polarization**	**Unchanged**

IV. CONCLUSION

In this article, a new method of designing the miniaturized multiband SC-FSS is presented, which is insensitive to almost all angles and all polarizations built upon the multiorder strong coupling resonance structures. First, a high-selectivity single-passband SC-FSS with two stopbands at both ends of the passband is developed by introducing two kinds of strong coupling resonance structures. Afterward, a dual-passband SC-FSS is realized by adding an extra inductive layer developed upon the single passband. The distributions of electric field and surface current are presented for further understanding and analyzing the physical mechanism of each band produced. Moreover, the ECM is also proposed and simulated to characterize the designed structures. Finally, a prototype of the dual-passband SC-FSS is measured to verify the proposed methodology. A good agreement is obtained between the measurement results and simulation ones by CST and ECM. Especially, the transmission poles and zeros do not change at all under the full polarizations, even when the incident angle increases to 86°. All results demonstrate that the proposed multiband SC-FSS is insensitive to almost all angles and all polarizations, which can be well applied to high-performance antenna radomes, antenna reflectors, and EMI shielding.

REFERENCES

[1] T. K. Wu, *Frequency-Selective Surface and Grid Array*. New York, NY, USA: Wiley, 1995.
[2] B. A. Munk, *Frequency Selective Surfaces: Theory and Design*. New York, NY, USA: Wiley, 2000.

[3] I. S. Syed, Y. Ranga, L. Matekovits, K. P. Esselle, and S. G. Hay, "A single-layer frequency-selective surface for ultrawideband electromagnetic shielding," *IEEE Trans. Electromagn. Compat.*, vol. 56, no. 6, pp. 1404–1411, Dec. 2014.

[4] G.-Q. Luo, W. Hong, Q.-H. Lai, K. Wu, and L.-L. Sun, "Design and experimental verification of compact frequency-selective surface with quasi-elliptic bandpass response," *IEEE Trans. Microw. Theory Techn.*, vol. 55, no. 12, pp. 2482–2487, Dec. 2007.

[5] L. Alonso-Gonzalez, S. Ver-Hoeye, M. Fernandez-Garcia, and F. Las Heras Andres, "Layer-to-layer angle interlock 3D woven bandstop frequency selective surface," *Prog. Electromagn. Res.*, vol. 162, pp. 81–94, 2018.

[6] T.-W. Deng, Y.-F. Yu, Z.-X. Shen, and Z.-N. Chen, "Design of 3-D multilayer ferrite-loaded frequency-selective rasorbers with wide absorption bands," *IEEE Trans. Microw. Theory Techn.*, vol. 67, no. 1, pp. 2474–2481, Jan. 2019.

[7] Q. Chen, D. Sang, M. Guo, and Y. Fu, "Frequency-selective rasorber with interabsorption band transparent window and interdigital resonator," *IEEE Trans. Antennas Propag.*, vol. 66, no. 8, pp. 4105–4114, Aug. 2018.

[8] G.-B. Wu, S.-W. Qu, Y.-X. Wang, and S. Yang, "Nonuniform FSS-backed reflectarray with synthesized phase and amplitude distribution," *IEEE Trans. Antennas Propag.*, vol. 66, no. 12, pp. 6883–6892, Dec. 2018.

[9] A. Chatterjee and S. K. Parui, "Beamwidth control of omnidirectional antenna using conformal frequency selective surface of different curvatures," *IEEE Trans. Antennas Propag.*, vol. 66, no. 6, pp. 3225–3230, Jun. 2018.

[10] T. Li, D. Li, L. Zhou, and E. Li, "Miniaturised FSS structure with excellent angular stability based on strong coupling for millimetre-wave communication," *Electron. Lett.*, vol. 54, no. 8, pp. 511–513, Apr. 2018.

[11] A. Abbaspour-Tamijani, K. Sarabandi, and G. M. Rebeiz, "Antenna–filter–antenna arrays as a class of bandpass frequency-selective surfaces," *IEEE Trans. Microw. Theory Techn.*, vol. 52, no. 8, pp. 1781–1789, Aug. 2004.

[12] B. Li and Z. Shen, "Synthesis of quasi-elliptic bandpass frequency-selective surface using cascaded loop arrays," *IEEE Trans. Antennas Propag.*, vol. 61, no. 6, pp. 3053–3059, Jun. 2013.

[13] M. Yan *et al.*, "A miniaturized dual-band FSS with second-order response and large band separation," *IEEE Antennas Wireless Propag. Lett.*, vol. 14, pp. 1602–1605, 2015.

[14] M. Yan *et al.*, "A quad-band frequency selective surface with highly selective characteristics," *IEEE Microw. Wireless Compon. Lett.*, vol. 26, no. 8, pp. 562–564, Aug. 2016.

[15] M. Yan *et al.*, "A tri-band, highly selective, bandpass FSS using cascaded multilayer loop arrays," *IEEE Trans. Antennas Propag.*, vol. 64, no. 5, pp. 2046–2049, May 2016.

[16] K. Payne, K. Xu, and J. H. Choi, "Generalized synthesized technique for the design of thickness customizable high-order bandpass frequency-selective surface," *IEEE Trans. Microw. Theory Techn.*, vol. 66, no. 11, pp. 4783–4793, Nov. 2018.

[17] J. Romeu and Y. Rahmat-Samii, "Fractal FSS: A novel dual-band frequency selective surface," *IEEE Trans. Antennas Propag.*, vol. 48, no. 7, pp. 1097–1105, Jul. 2000.

[18] Y. Li, L. Li, Y. Zhang, and C. Zhao, "Design and synthesis of multilayer frequency selective surface based on antenna-filter-antenna using minkowski fractal structures," *IEEE Trans. Antennas Propag.*, vol. 63, no. 1, pp. 133–141, Jan. 2015.

[19] T. Li *et al.*, "A novel miniaturized strong-coupled FSS structure with excellent angular stability," *IEEE Trans. Electromagn. Compat.*, vol. 63, no. 1, pp. 38–45, Feb. 2021, doi: 10.1109/TEMC.2020.3018558.

[20] M. N. Hussein, J. Zhou, Y. Huang, M. Kod, and A. P. Sohrab, "A miniaturized low-profile multilayer frequency-selective surface insensitive to surrounding dielectric materials," *IEEE Trans. Microw. Theory Techn.*, vol. 65, no. 12, pp. 4851–4860, Dec. 2017.

[21] D. Li, Z. Shen, and E.-P. Li, "Spurious-free dual-band bandpass frequency-selective surfaces with large band ratio," *IEEE Trans. Antennas Propag.*, vol. 67, no. 2, pp. 1065–1072, Feb. 2019.

[22] Z. Shen, J. Wang, and B. Li, "3-D frequency selective rasorber: Concept, analysis, and design," *IEEE Trans. Microw. Theory Techn.*, vol. 64, no. 10, pp. 3087–3096, Oct. 2016.

[23] D. Li, T.-W. Li, E.-P. Li, and Y.-J. Zhang, "A 2.5-D angularly stable frequency selective surface using via-based structure for 5G EMI shielding," *IEEE Trans. Electromagn. Compat.*, vol. 60, no. 3, pp. 768–775, Jun. 2018.

[24] T. Hussain, Q. Cao, J. K. Kayani, and I. Majid, "Miniaturization of frequency selective surfaces using 2.5-D knitted structures: Design and synthesis," *IEEE Trans. Antennas Propag.*, vol. 65, no. 5, pp. 2405–2412, May 2017.

[25] L. Shen, S. Long, M. Allerding, and M. Walton, "Resonant frequency of a circular disc, printed-circuit antenna," *IEEE Trans. Antennas Propag.*, vol. 25, no. 4, pp. 595–596, Jul. 1977.

[26] D. Li *et al.*, "A low-profile broadband bandpass frequency selective surface with two rapid band edges for 5G near-field applications," *IEEE Trans. Electromagn. Compat.*, vol. 59, no. 2, pp. 670–676, Apr. 2017.

[27] G. Xu, G. V. Eleftheriades, and S. V. Hum, "Generalized synthesis technique for high-order low-profile dual-band frequency selective surfaces," *IEEE Trans. Antennas Propag.*, vol. 66, no. 11, pp. 6033–6042, Nov. 2018.

[28] G. Xu, S. V. Hum, and G. V. Eleftheriades, "A technique for designing multilayer multistopband frequency selective surfaces," *IEEE Trans. Antennas Propag.*, vol. 66, no. 2, pp. 780–789, Feb. 2018.

[29] H. Johnson, and M. Graham, *High-Speed Signal Propagation: Advanced Black Magic*. Upper Saddle River, NJ, USA: Prentice-Hall, 2003.

Tian-Wu Li received the B.S. degree in communication engineering from the School of Mechanical, Electrical and Information Engineering, Shandong University, Weihai, China, in 2016. He is currently pursuing the Ph.D. degree in electronics science and technology with Zhejiang University, Hangzhou, China.

His current research interests focus on frequency-selective surface, metamaterial, metasurface, and EMC/electromagnetic interference (EMI) design in communication systems and chips.

Yu-Di Fan received the B.Eng. degree in information and communication engineering from the College of Information Science and Electronic Engineering, Zhejiang University, Hangzhou, China, in 2019, where he is currently pursuing the Ph.D. degree.

His current research interests focus on absorbers, metamaterials, and metasurfaces.

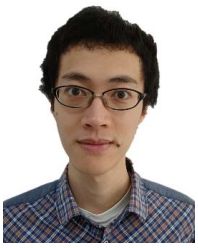

Yi-Jie Gu received the B.Eng. degree from the College of Information Science and Electronic Engineering, Zhejiang University, Hangzhou, China, in 2017. He is currently pursuing the Ph.D. degree in electronics science and technology with Zhejiang University.

His current research interests focus on spoof surface plasmons, metamaterials, and metasurfaces.

Shi-Yun Zhou received the B.S. degree in electromagnetic field and wireless technology from the University of Electronic Science and Technology of China, Chengdu, China, in 2016. She is currently pursuing the Ph.D. degree in electronics science and technology with Zhejiang University, Hangzhou, China.

Her current research interests focus on metamaterial, metasurface, and EMC/electromagnetic interference (EMI) design in the communication system and chip.

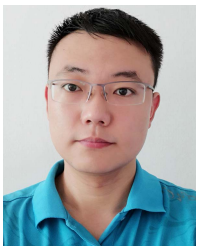

Peng-Fei Qin received the B.Eng. and Ph.D. degrees from the College of Information Science and Electronic Engineering, Zhejiang University, Hangzhou, China, in 2014 and 2020, respectively.

In May 2018, he was a Visiting Student with the Singapore University of Technology and Design, Singapore, for four months. His current research interests focus on metamaterials, metasurfaces, and spoof surface plasmons.

Da Li received the B.S. and Ph.D. degrees in electrical engineering from Zhejiang University, Hangzhou, China, in 2014 and 2019, respectively.

In 2017, he joined Nanyang Technological University, Singapore, as a Project Researcher. He currently works at China Electronics Technology Group Corporation 14th Research Institute, Nanjing, China. His current research interests include 5G antenna arrays, frequency-selective structures, and electromagnetic compatibility.

Wei E. I. Sha (Senior Member, IEEE) received the B.S. and Ph.D. degrees in electronic engineering from Anhui University, Hefei, China, in 2003 and 2008, respectively.

From July 2008 to July 2017, he was a Post-Doctoral Research Fellow and then a Research Assistant Professor with the Department of Electrical and Electronic Engineering, The University of Hong Kong, Hong Kong. From March 2018 to March 2019, he worked at University College London as a Marie Skłodowska-Curie Individual Fellow. In October 2017, he joined the College of Information Science and Electronic Engineering, Zhejiang University, Hangzhou, China, where he is currently a tenure-tracked Assistant Professor. He has authored or coauthored 150 refereed journal papers, 135 conference publications (including 38 invited talks), eight book chapters, and two books. His Google Scholar citation is 6500 with H-index of 39. His research interests include theoretical and computational research in electromagnetics and optics, focusing on the multiphysics and interdisciplinary research. His research involves fundamental and applied aspects in computational and applied electromagnetics, nonlinear and quantum electromagnetics, micro- and nano-optics, optoelectronic device simulation, and multiphysics modeling.

Dr. Sha is a member of the Optical Society of America (OSA). He received six Best Student Paper Prizes and one Young Scientist Award with his students. He served as a reviewer for 60 technical journals and a technical program committee members of nine IEEE conferences. He also served as an Associate Editors for IEEE JOURNAL ON MULTISCALE AND MULTIPHYSICS COMPUTATIONAL TECHNIQUES, IEEE OPEN JOURNAL OF ANTENNAS AND PROPAGATION, and IEEE ACCESS. In 2015, he was awarded the Second Prize of Science and Technology from Anhui Province Government, China. In 2007, he was awarded the Thousand Talents Program for Distinguished Young Scholars of China.

Er-Ping Li (Fellow, IEEE) received the Ph.D. degree in electrical engineering from Sheffield Hallam University, Sheffield, U.K., in 1992.

He is currently a Qiushi Chair Professor at the Department of Information Science and Electronic Engineering, Zhejiang University, Hangzhou, China, and the Dean of the Joint Institute of Zhejiang University–University of Illinois at Urbana–Champaign. Since 1989, he has been a Research Fellow, a Principal Research Engineer, an Associate Professor, and the Technical Director of the Singapore Research Institute and University. In 2000, he joined the Institute of High Performance Computing, A∗STAR, Singapore, as a Principal Scientist and the Director. His research interests include electrical modeling and design of microscale/nanoscale integrated circuits, 3-D electronic package integration, and nanoplasmonic technology.

Dr. Li is a fellow of the MIT Electromagnetics Academy, USA. He is also a Founding Member of the IEEE MTT-RF Nanotechnology Committee. He was a recipient of the 2015 IEEE Richard Stoddard Award on EMC, the IEEE EMC Technical Achievement Award, the Singapore IES Prestigious Engineering Achievement Award, the Changjiang Chair Professorship Award from the Ministry of Education in China, and a number of best paper awards. He was elected to the IEEE EMC Distinguished Lecturer in 2007. He served as an Associate Editor for the IEEE MICROWAVE AND WIRELESS COMPONENTS LETTERS from 2006 to 2008 and a Guest Editor for the 2006 and 2010 IEEE TRANSACTIONS ON ELECTROMAGNETIC COMPATIBILITY Special Issues and the 2010 IEEE TRANSACTIONS ON MICROWAVE THEORY AND TECHNIQUES APMC Special Issue. He is also an Associate Editor of the IEEE TRANSACTIONS ON ELECTROMAGNETIC COMPATIBILITY and IEEE TRANSACTIONS ON COMPONENTS, PACKAGING AND MANUFACTURING TECHNOLOGY. He has been a general chair and a technical chair for many international conferences. He was the President of the 2006 International Zurich Symposium on EMC, the Founding General Chair of the Asia-Pacific EMC Symposium, and the General Chair of the 2008, 2010, 2012, 2016 APEMC, and 2010 IEEE Symposium on Electrical Design for Advanced Packaging Systems. He has been invited to give numerous invited talks and plenary speeches at various international conferences and forums.